

RESEARCH ARTICLE

10.1002/2017JA023971

Key Points:

- Traveling ionospheric disturbances appeared at Indian east coast before ~90 min of the arrival of 26 December 2004 Sumatra tsunami
- Identification of the generation mechanism of tsunami traveling ionospheric disturbances that propagated ahead of Sumatra tsunami
- Proposing an alternative tool to monitor the offshore ahead of tsunami traveling ionospheric disturbances

Correspondence to:

M. S. Bagiya,
bagiyamala@gmail.com;
mala@iigs.iigm.res.in

Citation:

Bagiya, M. S., E. A. Kherani, P. S. Sunil, A. S. Sunil, S. Sunda, and D. S. Ramesh (2017), Origin of the ahead of tsunami traveling ionospheric disturbances during Sumatra tsunami and offshore forecasting, *J. Geophys. Res. Space Physics*, 122, 7742–7749, doi:10.1002/2017JA023971.

Received 30 JAN 2017

Accepted 28 JUN 2017

Accepted article online 11 JUL 2017

Published online 21 JUL 2017

Origin of the ahead of tsunami traveling ionospheric disturbances during Sumatra tsunami and offshore forecasting

Mala S. Bagiya¹ , E. A. Kherani² , P. S. Sunil¹ , A. S. Sunil¹ , S. Sunda³ , and D. S. Ramesh¹

¹Indian Institute of Geomagnetism (DST), Navi Mumbai, India, ²Instituto Nacional de Pesquisas Espaciais (INPE), São José dos Campos, Brazil, ³Space Application Centre (ISRO), Ahmedabad, India

Abstract The presence of ionospheric disturbances associated with Sumatra 2004 tsunami that propagated ahead of tsunami itself has previously been identified. However, their origin remains unresolved till date. Focusing on their origin mechanism, we document these ionospheric disturbances referred as Ahead of tsunami Traveling Ionospheric Disturbances (ATIDs). Using total electron content (TEC) data from GPS Aided GEO Augmented Navigation GPS receivers located near the Indian east coast, we first confirm the ATIDs presence in TEC that appear ~90 min ahead of the arrival of tsunami at the Indian east coast. We propose here a simulation study based on tsunami-atmospheric-ionospheric coupling that considers tsunamigenic acoustic gravity waves (AGWs) to excite these disturbances. We explain the ATIDs generation based on the dissipation of transverse mode of the primary AGWs. The simulation corroborates the excitation of ATIDs with characteristics similar to the observations. Therefore, we offer an alternative theoretical tool to monitor the offshore ATIDs where observations are either rare or not available and could be potentially important for the tsunami early warning.

1. Introduction

The 26 December 2004 Sumatra megathrust (~15 m maximum slip) earthquake (M_w 9.1–9.3) [Lay et al., 2005; Banerjee et al., 2007] generated the most devastating tsunami (maximum intensity of ~6.5 m) in history and the largest ever recorded in the offshore region of northwestern Sumatra so far. Figure 1 represents the simulated tsunami wave amplitude and travel time contours generated using satellite altimetry data by Sladen and Hebert [2008]. The tsunami water waves evolved ~1.00 UT near the epicentral region and they arrived at ~3.00 UT near the Indian coast. The inset in Figure 1 represents the coseismic slip due to this giant earthquake that ruptured ≥ 1300 km length and ≤ 150 km width down to a depth of 60 km of curved plate boundary toward north of epicenter [Ishii et al., 2005]. The horizontal (red vectors) and upward (blue vectors) surface displacements resulted from the earthquake exceeded ~4.5 m and ~2.5 m, respectively, at sites in northern Sumatra-Nicobar Islands and the source region. This was mainly responsible for the strong energy release and initial tsunami excitation which extended 600 to 800 km north of the epicenter terminating near the Nicobar Islands with a speed of 2.8 km/s [Ishii et al., 2005; Banerjee et al., 2007].

The Sumatra tsunami event has also offered opportunity to study the seismogenic and tsunamigenic disturbances in the overlying space, particularly in the ionosphere, and they are referred as Co-seismic Traveling Ionospheric Disturbances (CTIDs) [Artru et al., 2004; Heki and Ping, 2005]. During a tsunami, the overlying ionosphere can be disturbed by the acoustic gravity waves (AGWs) that arise from the earthquake hypocenter, associated Rayleigh waves, and the propagating tsunami waves [Heki et al., 2006].

Several studies reported CTIDs in total electron content (TEC) observations during the Sumatra tsunami [Heki et al., 2006; Astafyeva and Afraimovich, 2006; Liu et al., 2006a, 2006b; Lognonne et al., 2006; Otsuka et al., 2006; Choosakul et al., 2009] and also have been well reproduced using numerical modeling [Heki et al., 2006; Otsuka et al., 2006; Occhipinti et al., 2006; Shinagawa et al., 2007; Mai and Kiang, 2009].

Dasgupta et al. [2006] reported the presence of tsunami-induced ionospheric disturbances in GPS TEC observations at the Indian coast about 90 min prior to the 2004 Sumatra actual tsunami arrival. Such TEC disturbances are reported during 11 March 2011 Japan tsunami [e.g., Rolland et al., 2011], and they are found to propagate with acoustic speed in the range between 600 m/s and 1.4 km/s, similar to that noted by Dasgupta et al. [2006] for the Sumatra event. In recent simulation study of Japan event by Kherani et al. [2016],

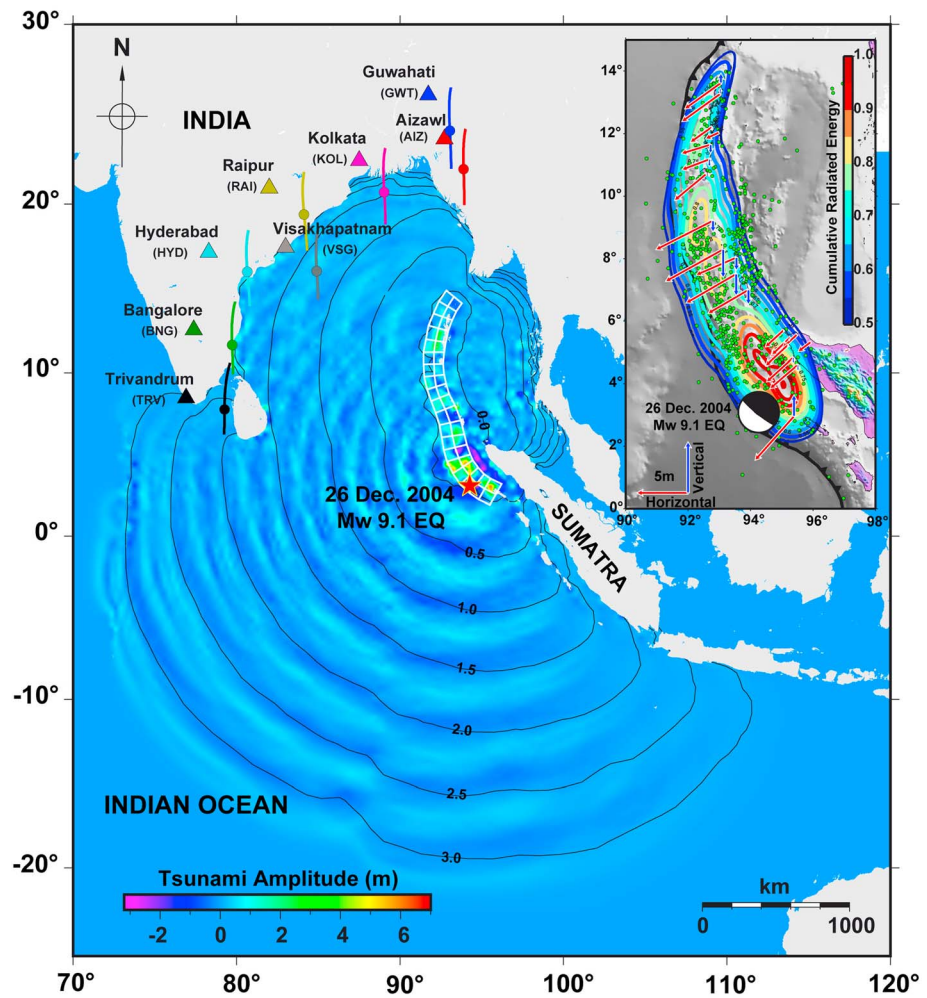


Figure 1. Sumatra tsunami amplitude map with travel time shown by contours in 30 min time interval. Red star indicates the 26 December 2004 earthquake epicenter and white grids indicate rupture model by *Sladen and Hebert* [2008]. The IPP trajectories projected at 350 km altitude for PRN 19 are also shown for eight receivers with their locations marked by triangles. The circles in trajectories represent the IPP location at 45 min, at maximum amplitudes in $\Delta\text{TEC}_{\text{obs}}$, from the beginning time of tsunami. The inset shows the Sumatra earthquake’s focal mechanism solution in beach ball, aftershock in green circles from U.S. Geological Survey (USGS), GPS observed coseismic horizontal and vertical land deformation in red and blue velocity vectors, respectively [*Banerjee et al.*, 2007], and cumulative radiated energy in contours [*Ishii et al.*, 2005] during this megathrust earthquake event.

these disturbances are referred as Ahead of tsunami Traveling Ionospheric Disturbances (ATIDs) and shown to be associated with the dissipated AGWs dynamics excited by the principal wavefront of propagating tsunami. While *Dasgupta et al.* [2006] are content with the recorded observations, in the present study, we go a step ahead and instead focus on the mechanism of their origin. In such a first attempt, we present here a simulation study of tsunami-induced AGWs in the atmosphere and its interaction with ionospheric plasma based on tsunami-atmosphere-ionosphere (TAI) coupling mechanism, on similar lines proposed by *Heki and Ping* [2005] and simulated by *Kherani et al.* [2016]. Based on the obtained reasonably good agreement between the observation and simulation, we term these TEC disturbances as ATIDs. We also discuss the strength and utility of GPS TEC observations as well as of simulation study in establishing an early warning system for tsunami.

2. Data Presentation

The 26 December 2004 Sumatra earthquake (onset time = 00:58:53 UT) was the first great magnitude seismic event to occur since the advent of modern space geodesy. We present here GPS TEC measurements on the

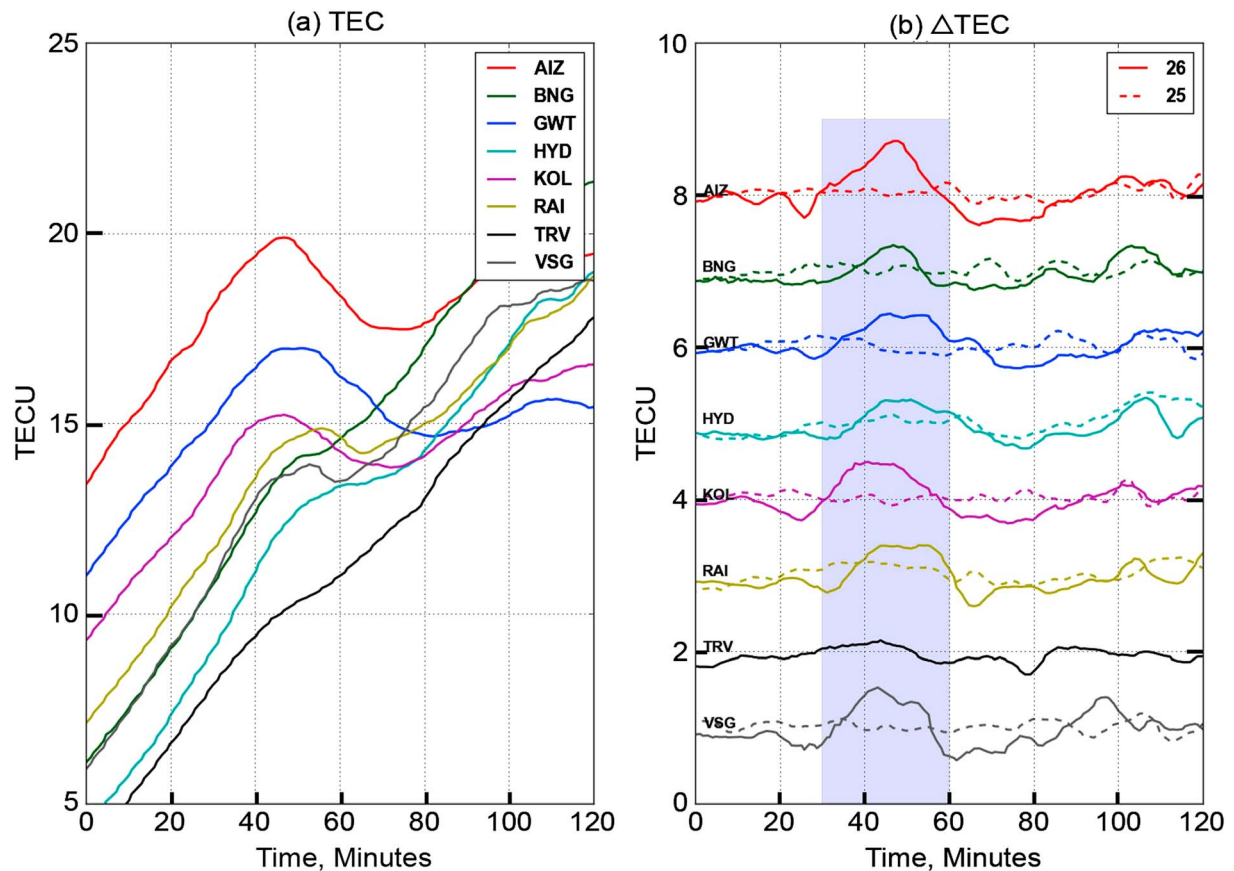


Figure 2. (a) TEC variations as observed by PRN 19 along the IPP trajectories from 8 GAGAN GPS stations (Figure 1) and (b) detrended $\Delta\text{TEC}_{\text{obs}}$ for the same IPP trajectories. $\Delta\text{TEC}_{\text{obs}} = \text{TEC} - \text{TEC}_{\text{avg}}$, where TEC_{avg} is the 30 min running average of TEC. The vertical axis for $\Delta\text{TEC}_{\text{obs}}$ is artificially shifted for better presentation. The time axis is zeroed with respect to the tsunami origin time (00:58 UT) and represents the average time in each running average window. The evolution of TEC disturbances could be observed at all stations within ~ 30 min from tsunami onset time. Long-period envelope of ~ 60 min could be clearly elucidated in $\Delta\text{TEC}_{\text{obs}}$. The similar signatures are absent in previous day $\Delta\text{TEC}_{\text{obs}}$ (25 December 2004).

earthquake day from eight GPS Aided GEO Augmented Navigation (GAGAN) receivers [Aizawl (AIZ), Bangalore (BNG), Guwahati (GWT), Hyderabad (HYD), Kolkata (KOL), Raipur (RAI), Trivandrum (TRV), and Visakhapatnam (VSG)] located near the Indian east coast. The distribution of GPS receivers is represented by triangles in Figure 1. Figure 1 also depicts ionospheric piercing point (IPP) trajectories at 350 km altitude between 01:00 UT and 03:00 UT for PRN 19 from all GAGAN stations. The TEC disturbances, $\Delta\text{TEC}_{\text{obs}}$, are estimated by detrending TEC data (elevation mask $>20^\circ$) using a 30 min running average to block the slow variations with frequencies <0.5 mHz since the tsunamigenic TEC disturbances are known to occupy the frequencies >0.5 mHz [Rolland *et al.*, 2011]. Figure 2 shows the temporal variation of $\Delta\text{TEC}_{\text{obs}}$ as measured along the trajectories by PRN 19. We note the presence of amplified waveform variations with wide temporal envelope of around 60 min that appear almost simultaneously at all GAGAN stations within ~ 30 min after the tsunami onset. As evident such waveform is absent on previous day (25 December 2004) (Figure 2b). The tsunami travel time diagram in Figure 1 confirms that these waveform or disturbances appear around 90 min earlier than the tsunami arrival at Indian east coast. Their amplitudes range from 0.3 to 0.7 total electron content unit, $1 \text{ TECU} = 10^{16} \text{ el m}^{-2}$ with minimum and maximum disturbances registered at TRV and AIZ, respectively. We also note that the IPP positions of the satellites are at overhead of corresponding receivers during the detection of these disturbances. The observed characteristics of ATIDs are similar to those reported by Dasgupta *et al.* [2006] and also similar to the ATIDs reported during the Japan tsunami [Kherani *et al.*, 2016]. Also, they are different from the earlier reported near-field and far-field coseismic TEC disturbances which appeared after 10–15 min and 2–7 h of the Sumatra 2004 earthquake, respectively [Heki *et al.*, 2006; Astafyeva and Aframovich, 2006].

The $\Delta\text{TEC}_{\text{obs}}$, in the present study, may arise from either of three kinds of forcing: hypocenter, associated Rayleigh wave, and tsunami propagation [Heki *et al.*, 2006]. However, unlike the observed characteristics from Figure 2, the disturbances from hypocenter forcing are mostly confined around the rupture [Heki *et al.*, 2006] while the disturbances from Rayleigh wave forcing are expected to appear within 10 min (after the earthquake onset) at the Indian east coast, as they propagate with a velocity of about 3.5 km/s [Artru *et al.*, 2004]. In contrast to these possibilities, the forcing from tsunami propagation, which has successfully explained the CTIDs [Ochchipinti *et al.*, 2006], is more probable scenario to be explored. Moreover, based on this forcing, Kherani *et al.* [2016] have explained CTIDs/ATIDs observed during the Japan tsunami. The next section describes the proposition adopted by us to identify the origin mechanism/s that is/are responsible for the observed Sumatra ATIDs.

3. Synthetic ATIDs From the TAI Simulation Model

The ATIDs of similar characteristics are reported during Tohoku tsunami and they are observed to propagate with speed of ~600 m/s to 1.4 km/s, much faster than the tsunami [Kherani *et al.*, 2016]. We proposed, for the first time, the identical simulation approach to characterize the Sumatra 2004 tsunami-associated ATIDs. The simulation results are carried out using TAI coupled model of Kherani *et al.* [2016].

The following set of governing equations of AGWs, as presented by Kherani *et al.* [2016], is employed:

$$\frac{\partial^2 \vec{W}}{\partial t^2} = \frac{1}{\rho} \nabla (\gamma p \nabla \cdot \vec{W}) - \frac{\nabla p}{\rho^2} \nabla \cdot (\rho \vec{W}) + \frac{1}{\rho} \nabla (\vec{W} \cdot \nabla) p + \frac{\partial}{\partial t} (\nu \nabla^2 \vec{W} + (\zeta' + \frac{\nu}{3}) \nabla (\nabla \cdot \vec{W})) - \frac{\partial}{\partial t} (\vec{W} \cdot \nabla \vec{W}), \quad (1)$$

$$\frac{\partial p}{\partial t} + \nabla \cdot (\rho \vec{W}) = 0, \quad (2)$$

$$\frac{\partial p}{\partial t} + (\vec{W} \cdot \nabla) p + \gamma p \nabla \cdot \vec{W} = 0, \quad (3)$$

where W , ρ , $p = \rho RT$, and T are the wind amplitude of AGWs, atmospheric density, pressure, and temperature respectively. Here $\nu = \mu/\rho$ and $\zeta' = \zeta/\rho$ are the first and second kinematic viscosities and μ , ζ are the first and second dynamic viscosities. To simulate the ionospheric TEC, the following hydromagnetic equations in the ionosphere are employed [Kherani *et al.*, 2016]:

$$\frac{\partial \vec{u}_s}{\partial t} = \frac{q_s}{m_s} (\vec{E} + \vec{u}_s \times \vec{B}_o) - \nu_s \vec{u}_s + \nu_s \vec{W}, \quad (4)$$

$$\frac{\partial n_s}{\partial t} + \nabla \cdot (n_s \vec{u}_s) = P - L, \quad (5)$$

$$\nabla^2 \vec{E} - \nabla (\nabla \cdot \vec{E}) - \frac{1}{c^2} \frac{\partial^2 \vec{E}}{\partial t^2} - \mu_0 \frac{\partial \vec{J}}{\partial t} = 0, \quad (6)$$

$$\vec{J} = \underline{\sigma} \cdot \vec{E} + \vec{J}_\omega; \vec{J}_\omega = e (n_i \vec{u}_i^\omega - n_e \vec{u}_e^\omega). \quad (7)$$

Here n_s , u_s are the number density and velocity of plasma fluid s ; ($s = \text{ions}(i)/\text{electrons}(e)$), ($q_i = +Ze$, $q_e = -e$, $Z_i = 1$), and (\vec{E}, \vec{J}) are the electric field and net ionospheric current; $(\vec{u}_i^\omega, \vec{u}_e^\omega)$ are the ion/electron velocities without the electric field as derived from equation (4); J_ω is the corresponding ionospheric current density; ν_s is the frequency of collision between species s to neutral; \vec{B}_o is the Earth's magnetic field; $\underline{\sigma}$ is the ionospheric conductivity tensor; and $(c = \frac{1}{\sqrt{\mu_0 \epsilon_0}})$ is the speed of light in vacuum. (P , L) are the production and loss of ions and electrons by photoionization and chemical reactions. The production

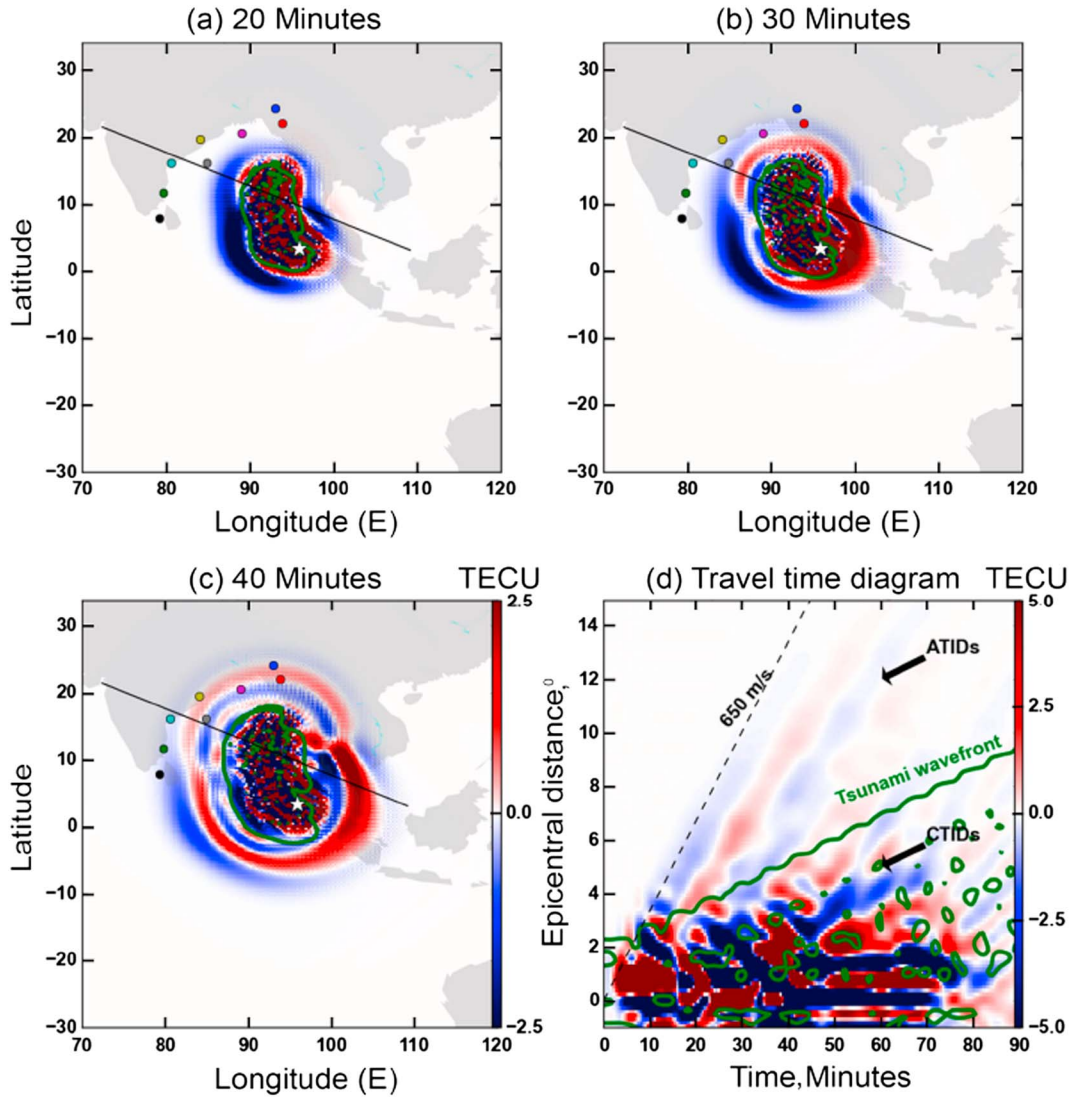


Figure 3. Simulated ionospheric response to tsunamigenic AGWs. (a–c) Simulated $\Delta\text{TEC}_{\text{sim}}$ (represented by color pixmap) at 20, 30, and 40 min after the tsunami onset. The green contours in Figures 3a–3c represent the tsunami wavefronts. The black line in Figures 3a–3c represents the cross section along which the travel time diagram is constructed and presented in Figure 3d. (d) The color pixmap and green contours represent the $\Delta\text{TEC}_{\text{sim}}$ and tsunami propagations along the black line in Figures 3a–3c. In addition, a dashed line with slope = 650 m/s is also plotted in Figure 3d, which determines the propagation velocity of ATIDs. $\Delta\text{TEC}_{\text{sim}}$ in the present study is defined as $\text{TEC}_w(t) - \text{TEC}_o(t)$, where TEC_w and TEC_o are estimated from the ionospheric density obtained by solving the continuity equation with and without the presence of AGWs. The circles in Figures 3a–3c indicate the IPP of maximum amplitudes in $\Delta\text{TEC}_{\text{obs}}$ from the beginning time of tsunami.

term P in equation (5) is derived from SAMI2 model [Huba *et al.*, 2000]. The chemical loss term, L , in equation (5) is retained through effective recombination rate as taken by Kherani *et al.* [2016]. In addition to the wave equation (equation (6)), \vec{E} also satisfies the charge neutrality condition given by the following equation [Kherani *et al.*, 2016]:

$$\nabla \cdot \vec{J} = 0 \text{ Or } \nabla \cdot (\sigma \cdot \vec{E} + \vec{J}_\omega) = 0 \Rightarrow \nabla \cdot \vec{E} = -\sigma^{-1} (\vec{E} \cdot \nabla \sigma + \nabla \cdot \vec{J}_\omega). \quad (8)$$

The tsunami wavefield modeled by Sladen and Hebert [2008] is employed as the vertical forcing input at all times at the lower boundary, i.e., at the ocean surface to the TAI model. The simulation volume is bounded in altitude, latitude, and longitude between 0 and 600 km, -35° to 35° , and 60°E to 130°E , respectively. The simulation begins at tsunami origin time $t = 00:58$ UT. The ambient atmospheric/ionospheric conditions are obtained from the longitude extended SAMI2 model of Huba *et al.* [2000] as presented by Sousasantos *et al.* [2013]. More detail on the TAI coupled model could be found in Kherani *et al.* [2012, 2016].

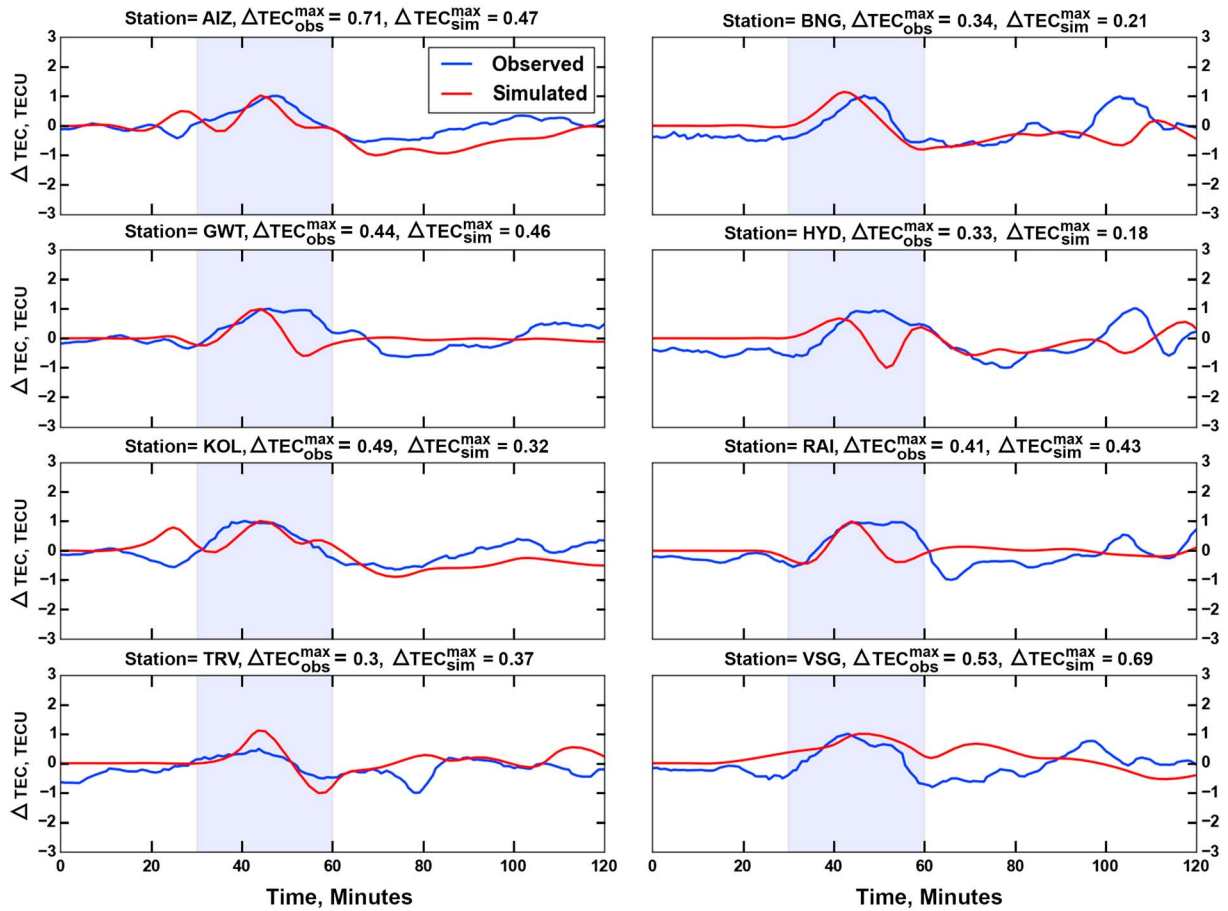


Figure 4. Comparison between the $\Delta\text{TEC}_{\text{obs}}$ (blue) and $\Delta\text{TEC}_{\text{sim}}$ (red). The panels show the comparison at all eight GPS stations. They are normalized to their respective maximum values as indicated at the top of each panel. The TIDs of interest, i.e., ATIDs, are highlighted in shaded region.

4. Results and Discussion

The simulation results at $t = 20, 30,$ and 40 min after the tsunami initiation are presented in Figures 3a–3c, respectively. In these figures, the simulated $\Delta\text{TEC}_{\text{sim}}$ and the tsunami wavefield are depicted as color image and green contours, respectively. The simulated ΔTEC is defined here as

$$\Delta\text{TEC}_{\text{sim}}(t) = \text{TEC}_w(t) - \text{TEC}_o(t)$$

TEC_w and TEC_o are estimated at each epoch from the ionospheric density by solving the continuity equation (equation (4)) with and without including the AGWs dynamics. This definition of $\Delta\text{TEC}_{\text{sim}}(t)$ is adopted since the ambient TEC itself is changing with time and in longitude due to the photoionization process. We note two kinds of TIDs here: one trailing and another preceding the tsunami. The preceding TIDs, i.e., ATIDs, arrive almost simultaneously within 40 min at all receiver locations near the Indian east coast.

To understand the origin and propagation characteristics of the simulated ATIDs, we construct a travel time diagram for the same as shown in Figure 3d. The travel time diagram represents that spatio-temporal variability of simulated TIDs (represented by color image) in horizontal cross section along the black line in Figures 3a–3c. The green contours in Figure 3d depicts the tsunami wavefronts while two wavefronts in simulated $\Delta\text{TEC}_{\text{sim}}(t)$ could be clearly discriminated, one traveling ahead of tsunami and one trailing behind the tsunami. The estimated spatial wavelengths of ATIDs lay between 1° and 2° . The propagation velocity of ATIDs from the slope of dotted line is ~ 650 m/s that resembles the velocity values derived using triangulation method at Indian coast [Dasgupta et al., 2006]. Moreover, this is consistent with the simulated ATIDs during Tohoku-Oki tsunami that were shown to have wave parameters in similar range.

As explained by *Kherani et al.* [2016], the simulated dynamics involve the excitations of primary AGWs from the tsunami forcing, their dissipation in the thermosphere, and subsequent generation of secondary AGWs in the thermosphere. Although both primary and secondary waves contribute to ATIDs, the dissipation of transverse mode of the primary waves is fundamentally responsible for their generation. In this process, the horizontal momentum associated with the transverse mode provides essential thrust (i.e., secondary forcing) for the generation of secondary waves and so for the ATIDs which then propagates dominantly horizontally due to the horizontal thrust. Moreover, the associated longitudinal secondary mode acquires longer (as compared to the primary) horizontal wavelength, leading to the faster speed (as compared to the tsunami) of ATIDs, equals to the acoustic speed in the thermosphere.

Finally, a comparison between normalized $\Delta\text{TEC}_{\text{obs}}$ (blue curves) and $\Delta\text{TEC}_{\text{sim}}$ (red curves) is shown in Figure 4 for all stations. The normalization factor corresponds to their respective maximum values. Here the $\Delta\text{TEC}_{\text{sim}}$ is shown along the same IPP trajectories (Figure 1) for which $\Delta\text{TEC}_{\text{obs}}$ (Figure 2) are obtained. We note that the simulated waveforms ($\Delta\text{TEC}_{\text{sim}}$) agree reasonably well with the corresponding observed ones at all receiver locations. In particular, the first broad peak during 30–60 min associated with ATIDs that is observed ~ 90 min prior to the tsunami arrival is simulated with reasonable success. Note that the actual $\Delta\text{TEC}_{\text{sim}}$ and $\Delta\text{TEC}_{\text{obs}}$ amplitudes differ and are denoted at the top of each panel in Figure 4. We assume that these differences could arise because of variance between empirical models derived input ambient atmospheric/ionospheric parameters used in simulation and those in realistic case besides the different methods employed to estimate the $\Delta\text{TEC}_{\text{obs}}$ and $\Delta\text{TEC}_{\text{sim}}$.

As mentioned in section 1, the ATIDs are earlier observed during Japan tsunami event when they appear as acoustic wavefront in the travel time diagram (TTD) [Rolland et al., 2011], an important characteristic of ATIDs. It has to be noted that this TTD was derived using dense GPS network. Our successful attempt to simulate the ATIDs in the present study suggests that the TAI coupled simulation can be employed to complement the observations to identify the ATIDs by constructing the simulated TTD (Figure 3d). Moreover, in the absence of offshore observations, the simulated ATIDs can complement the early warning system if the actual tsunami propagation is made available in real time. However, at this stage, this proposal is qualitative in nature since the tsunami height, which is an essential parameter for the early warning, remained to be derived from the $\Delta\text{TEC}_{\text{obs}}$.

5. Conclusion

Using 26 December 2004 Sumatra tsunami simulated parameters [Sladen and Hébert, 2008] as input to the TAI simulation model, we identify the generation mechanism of a new class of ionospheric disturbances, referred as ATIDs. The variations recorded in the TEC observed by the GAGAN receivers located near the Indian east coast 90 min prior to arrival of Sumatra tsunami are explained, for the first time, in terms of ATIDs. The ATIDs are explained based on the dissipation of transverse mode of the primary AGWs. The successful simulation of ATIDs based on TAI coupling model offers an alternative scenario to monitor the offshore ionosphere in the absence of offshore observations from the GNSS network. Further, real-time simulation of ATIDs can enhance the effectiveness of early tsunami warning system since they are recorded at the coastal GPS receivers much earlier than the tsunami arrival itself.

References

- Artru, J., T. Farges, and P. Lognonné (2004), Acoustic waves generated from seismic surface waves: Propagation properties determined from Doppler sounding observations and normal-mode modelling, *Geophys. J. Int.*, *158*, 1067–1077.
- Astafyeva, E. I., and E. L. Afraimovich (2006), Long-distance propagation of traveling ionospheric disturbances caused by the great Sumatra-Andaman earthquake on 26 December 2004, *Earth Planets Space*, *58*(8), 1025–1031.
- Banerjee, P., F. Pollitz, B. Nagarajan, and R. Bürgmann (2007), Coseismic slip distribution of the 26 December 2004 Sumatra-Andaman and 28 March 2005 Nias earthquakes from GPS static offsets, *Bull. Seismol. Soc. Am.*, *97*(1), S86–S102, doi:10.1785/0120050609.
- Choosakul, N., A. Saito, T. Iyemori, and M. Hashizume (2009), Excitation of 4-min periodic ionospheric variations following the great Sumatra-Andaman earthquake in 2004, *J. Geophys. Res.*, *114*, A10313, doi:10.1029/2008JA013915.
- DasGupta, A., A. Das, D. Hui, K. Kumar Bandyopadhyay, and M. R. Sivaraman (2006), Ionospheric perturbations observed by the GPS following the December 26th, 2004 Sumatra-Andaman earthquake, *Earth Planets Space*, *58*, 167–172.
- Heki, K., and J. Ping (2005), Directivity and apparent velocity of the coseismic ionospheric disturbances observed with a dense GPS array, *Earth Planet. Sci. Lett.*, *236*, 845–855, doi:10.1016/j.epsl.2005.06.010.
- Heki, K., Y. Otsuka, N. Choosakul, N. Hemmakorn, T. Komolmis, and T. Maruyama (2006), Detection of ruptures of Andaman fault segments in the 2004 great Sumatra earthquake with coseismic ionospheric disturbances, *J. Geophys. Res.*, *111*, B09313, doi:10.1029/2006GL028200.

Acknowledgments

We thank Anthony Sladen of GeoAzur for providing the simulated tsunami wavefield. EAK wishes to acknowledge financial support from FAPESP (Brazil) under 2011/21903-3. The GAGAN GPS data are available with SS. We thank Ajish P. Saji, K. Priyesh, T. Sreeraj and B. I. Panchal for extending their help during the formulation of this paper. This work is supported by Department of Science and Technology (DST), Government of India. This work is part of the new interdisciplinary initiative, Lithosphere-Atmosphere-Ionosphere-Magnetosphere (LAIM) coupling program, of Indian Institute of Geomagnetism, Navi Mumbai, India. SS duly acknowledges the support of the Airport Authority of India. We sincerely thank Robert J. Geller and anonymous reviewer for providing their insightful and constructive comments.

- Huba, J., G. Joyce, and J. Fedder (2000), Sami2 is another model of the ionosphere (SAMI2): A new low latitude ionosphere model, *J. Geophys. Res.*, *105*, 23,035–23,053.
- Ishii, M., P. M. Shearer, H. Houston, and E. Vidale (2005), Extent, duration and speed of the 2004 Sumatra Andaman earthquake imaged by the Hi-Net array, *Nature*, *436*, doi:10.1038/nature03675.
- Kherani, E. A., P. Lognonne, H. Hebert, L. Rolland, E. Astafyeva, G. Occhipinti, P. Coisson, D. Walwer, and E. R. de Paula (2012), Modelling of the total electronic content and magnetic field anomalies generated by the 2011 Tohoku-oki tsunami and associated acoustic-gravity waves, *Geophys. J. Int.*, *191*(3), 1049–1066.
- Kherani, E. A., L. Rolland, P. Lognonne, A. Sladen, V. Klausner, and E. R. de Paula (2016), Traveling ionospheric disturbances propagating ahead of the Tohoku-Oki tsunami: A case study, *Geophys. J. Int.*, *204*, 1148–1158, doi:10.1093/gji/ggv500.
- Lay, T., et al. (2005), The great Sumatra-Andaman earthquake of 26 December 2004, *Science*, *308*, 1127–1133.
- Liu, J. Y., Y. B. Tsai, S. W. Chen, C. P. Lee, Y. C. Chen, H. Y. Yen, and W. Y. Chang (2006a), Giant ionospheric disturbances excited by the M9.3 Sumatra earthquake of 26 December 2004, *Geophys. Res. Lett.*, *33*, L02103, doi:10.1029/2005GL023963.
- Liu, J. Y., Y. B. Tsai, K. F. Ma, Y. I. Chen, H. F. Tsai, C. H. Lin, M. Kamogawa, and C. P. Lee (2006b), Ionospheric GPS total electron content (TEC) disturbances triggered by the 26 December 2004 Indian Ocean tsunami, *J. Geophys. Res.*, *111*, A05303, doi:10.1029/2005JA011200.
- Lognonne, P., J. Artru, R. Garcia, F. Crespon, V. Ducic, E. Jeansou, G. Occhipinti, J. Helbert, G. Moreaux, and P.-E. Godet (2006), Ground-based GPS imaging of ionospheric post-seismic signal, *Planet. Space Sci.*, *54*(5), 528–554.
- Mai, C.-L., and J.-F. Kiang (2009), Modeling of ionospheric perturbation by 2004 Sumatra tsunami, *Radio Sci.*, *44*, RS3011, doi:10.1029/2008RS004060.
- Occhipinti, G., Lognonne Philippe, E. Alam Kherani, and H elene H ebert (2006), Three-dimensional waveform modeling of ionospheric signature induced by the 2004 Sumatra tsunami, *Geophys. Res. Lett.*, *33*, L20104, doi:10.1029/2006GL026865.
- Otsuka, Y., N. Kotake, T. Tsugawa, K. Shiokawa, T. Ogawa, S. S. Effendy, M. Kawamura, T. Maruyama, N. Hemmakorn, and T. Komolmis (2006), GPS detection of total electron content variations over Indonesia and Thailand following the 26 December 2004 earthquake, *Earth Planets Space*, *58*(2), 159–165.
- Rolland, L. M., P. Lognonn e, E. Astafyeva, E. A. Kherani, N. Kobayashi, M. Mann, and H. Munekane (2011), The resonant response of the ionosphere imaged after the 2011 off the Pacific coast of Tohoku earthquake, *Earth Planets Space*, *63*, 853–857.
- Shinagawa, H., T. Iyemori, S. Saito, and T. Maruyama (2007), A numerical simulation of ionospheric and atmospheric variations associated with the Sumatra earthquake on December 26, 2004, *Earth Planets Space*, *59*(9), 1015–1026.
- Sladen, A., and H. H ebert (2008), On the use of satellite altimetry to infer the earthquake rupture characteristics: Application to the 2004 Sumatra event, *Geophys. J. Int.*, *172*, 707–714.
- Sousasantos, J., E. A. Kherani, and J. H. A. Sobral (2013), A numerical simulation study of the collisional-interchange instability seeded by the pre-reversal vertical drift, *J. Geophys. Res. Space Physics*, *118*, 7438–7449, doi:10.1002/2013JA018803.